# Out-of-Distribution Nuclei Segmentation in Histology Imaging via Liquid Neural Networks with Modern Hopfield Layer

Bishal Ranjan Swain[1][0000−0001−7098−6870], Kyung Joo Cheoi[2][0000−0003−2076−9119], and Jaepil Ko[1](✉)[0000−0002−0625−092X]

[1] Kumoh National Institute of Technology, Gumi, Korea 39177
{bishalswain,nonezero}@kumoh.ac.kr
[2] Chungbuk National University, Cheongju, Korea 28644
kjcheoi@chungbuk.ac.kr

**Abstract.** Precise nuclei segmentation is crucial in histopathology but remains challenging due to variable tissue types, staining protocols, and imaging conditions. Traditional deep neural networks often perform inconsistently when presented with data distributions not seen during training. Existing approaches typically process multi-scale features sequentially but lack mechanisms to explicitly enforce robustness against distribution shifts. To address this, we propose a novel framework that integrates hierarchical feature learning with associative memory to enhance model adaptability. First, we extract multi-layer embeddings from an image encoder, then process them in reverse layer order (from deepest to shallowest) using Liquid Neural Network (LNN). This design allows the model to capture global features initially and then refine them with increasingly localized information. The image encoding and the LNN encoding is then concatenated in hidden space and passed through Hopfield layer that stabilizes and stores relevant patterns. This effectively enhances domain-invariant representations by filtering out spurious correlations. Our OOD experiments on nuclei segmentation benchmark datasets show that our approach achieves average improvement of 16.35% over baseline models. Our code will be released at https://github.com/CVPR-KIT/OOD-Nuclei-Segmentation-via-LNNs-with-MHN.

**Keywords:** Nuclei Segmentation · Instance Segmentation · Out-of-Distribution.

## 1 Introduction

Nuclei segmentation in histopathology images is a critical task for quantitative tissue analysis and diagnosis in digital pathology [17]. By delineating individual cell nuclei, automated systems can extract key morphological features – such as nuclear size, shape, and density – that help in disease gradation and prognosis [20]. Despite significant progress with modern image segmentation techniques,

accurate segmentation of nuclei remains challenging [6]. This is due to high variability in nuclear appearance and variability induced during slide preparation and image acquisition. Due to this, models often encounter out-of-distribution (OOD) data, where histology images differ from the training set in stain intensity, tissue type, or scanner settings. These differences can lead to significant drop in segmentation performance on external datasets and require re-training [20]. The data variations may include - minor staining deviations, tissue-specific morphology, different image and color profiles of acquisition devices. These problems give rise to domain shifts between training (source domain) and deployment (target domain) data. Such OOD scenarios pose a fundamental challenge: a model trained on one distribution of nuclei images may fail to generalize to unseen distributions of similar nuclei images, yielding incorrect segmentation and undermining its utility in real-world applications.

There have been continuous research and advancement in fully automated segmentation of nuclei regions. While semantic segmentation is used to calculate nuclei and disease area, instance segmentation identifies each nuclei as a separate entity within an image, allowing for detailed morphological studies [19]. For instance, fully convolutional architectures like U-Net [23] and its variants, have achieved excellent results in delineating nuclei when training. Despite these task-specific models displaying acceptable performance on the seen data from training distribution, they show difficulty in handling data from different distributions, especially for the nuclei with different shapes and stain environments [9, 14]. Several strategies have been explored to improve robustness in nuclei segmentation. Normalization-based methods adjust color and intensity distributions like stain normalization [26, 13] was applied to reduce inter-slide variability. Augmentation-based methods [27] apply stain-jitter and geometric transformations to introduce synthetic variability during training to expose the model to a broader input distribution. While these techniques can partially mitigate distribution gaps, they often require careful tuning and can introduce artifacts or inconsistent improvements. Unsupervised domain adaptation frameworks have also been proposed to align feature representations between a labeled source domain and an unlabeled target domain [28]. Approaches such as adversarial feature alignment [18] or image-to-image translation [29] can boost performance on a specific target domain, but they demand access to target data and require retraining. But, even then, it may not generalize to arbitrary unseen domains. More recently, adapting or utilizing foundational segmentation models like the Segment Anything Model (SAM) [16] have been proposed, aiming to provide universal segmentation capabilities across diverse and potentially out-of-distribution image domains, thereby motivating further exploration of generalizable segmentation methods [2, 25].

In this paper, we pursue a different direction to tackle OOD nuclei segmentation. We propose a novel network structure that leverages the adaptive dynamics of Liquid Neural Networks (LNNs) [12] and the associative memory of modern hopfield networks (MHN) [22]. LNNs are a class of continuous-time recurrent models inspired by neuromorphic principles, which maintain flexible,

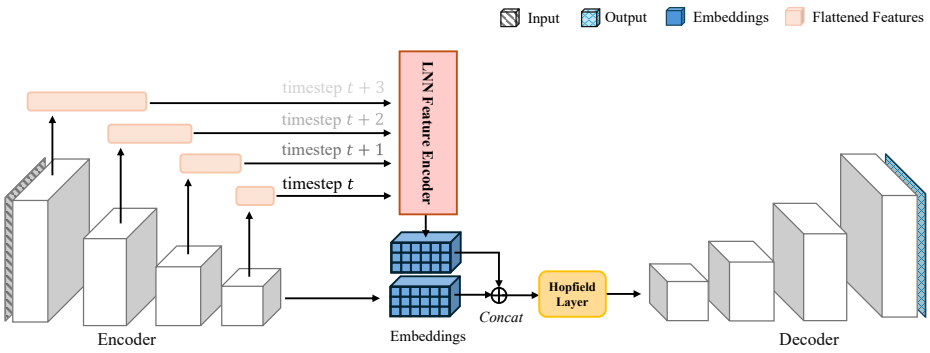


**Fig. 1.** The overall architecture of the proposed method

time-varying internal dynamics that can adapt to changing inputs even after training [5]. Unlike conventional feed-forward networks with fixed learned parameters, LNNs can adjust their behavior based on input sequences or conditions, effectively filtering out irrelevant features and focusing on salient patterns. This adaptivity suggests that LNN-based image encoders could better handle domain shifts, as demonstrated recently in [1]. We employ a modern hopfield layer that stores a set of representative nucleus feature embeddings learned during training. During inference, the MHN layer associates incoming features with the closest stored prototypes, essentially performing a content-based retrieval of familiar nuclear patterns. The retrieved patterns then influence the decoder's predictions, helping to correct segmentation outputs when the input exhibits OOD characteristics.

## 2 Methods

The overall architectural pipeline is shown in Fig. 1. Our proposed methodology first passes the input image through an encoder to obtain image encodings and its corresponding feature maps at multiple scales (from coarse high-level features to fine-grained details). These multi-scale feature embeddings are then treated as a sequential input to the LNN, in order from coarsest to finest scale. At each step, the LNN ingests the feature map of that scale and updates its hidden state. In this way, global context from low-resolution features is gradually refined by incorporating higher-resolution details over time. Next, we concatenate the image embeddings and the LNN output into a shared hidden representation and feed this into a MHN layer. Finally, the enriched features are decoded to generate the instance segmentation map.

### 2.1 LNN Feature Encoder

The central idea behind our LNN feature encoder is to mimic hierarchical visual reasoning. When analyzing a scene, humans first grasp the global context

and then progressively focus on finer details. Our LNN is designed to replicate this process by sequentially integrating multi-scale features - from the coarsest (most contextual) to the finest (most detailed). This temporal processing allows the model to build a rich, context-aware representation that is dynamically refined as more localized information becomes available. We implement the LNN using a Closed-form continuous-time model, specifically the Continuous-time forward-constraint (CfC) cell introduced in [11]. The CfC is a four-layer LNN architecture that provides numerical approximation of the closed-form solution of LTCs, avoiding the need for iterative ODE solvers. This makes it computationally efficient while retaining the expressiveness of continuous-time dynamics [5].

In our proposed method, the CfC cell serves to sequentially process the multi-scale encoder features. Formally, let $F^1, F^2, \ldots, F^T$ denote the encoder feature maps from $T$ scales (with $F^1$ the coarsest scale and $F^T$ the finest). Then we project each $F^t$ to a common hidden dimension (via $1 \times 1$ convolution), so that all inputs to the LNN have the same dimension. We flatten each projected feature map $F^t_{proj} \in \mathbb{R}^{B\times D\times H_t\times W_t}$ along its spatial dimensions into a sequence $x_t \in \mathbb{R}^{B\times(H_tW_t)\times D}$ and feed it to the CfC cell.

A core characteristic of CfC cells is the closed-form gating function that blends multiple learned transformations of the input $(x, I)$ based on a parameterized function $f$ multiplied by a continuous-time variable $t$. We can write the CfC update equations as:

$$x(t) \;=\; \sigma\Big(-f\big(x, I; \theta_f\big)\, t\Big) \;\odot\; g\big(x, I; \theta_g\big) \;+\; \Big[1 \;-\; \sigma\big(-f\big(x, I; \theta_f\big)\, t\big)\Big] \;\odot\; h\big(x, I; \theta_h\big), \tag{1}$$

where $\sigma(\cdot)$ is the sigmoid function; $f(\cdot;\theta_f)$, $g(\cdot;\theta_g)$, and $h(\cdot;\theta_h)$ are neural functions with learnable parameters $\theta_f, \theta_g, \theta_h$; $I$ denotes the current input (multi-scale feature map); and $\odot$ is element-wise multiplication. Intuitively, $f$ determines how quickly $x(t)$ transitions from the transformation $g$ to the transformation $h$, as it multiplies the time variable $t$ (set to 1 for equally spaced encoder scales) in the sigmoid argument. At large positive values, the sigmoid term goes to 1, favoring $g$, whereas at large negative values, it switches to $h$. This gating mechanism ensures a stable closed-form update of the hidden state, effectively capturing instantaneous dynamics of the system. After we get the output from the LNN we normalize it via $\ell_2$ normalization. Fig. 2 shows the CfC network used in the proposed methodology.

### 2.2 Hopfield Layer

While the LNN provides adaptive feature integration, large domain shifts could still cause it to produce anomalous or inconsistent representations [12]. To address this and enforce representational stability, we introduce a Modern Hopfield Network layer that functions as an associative memory. If the input feature vector deviates from known patterns, the Hopfield layer pulls it towards the closest

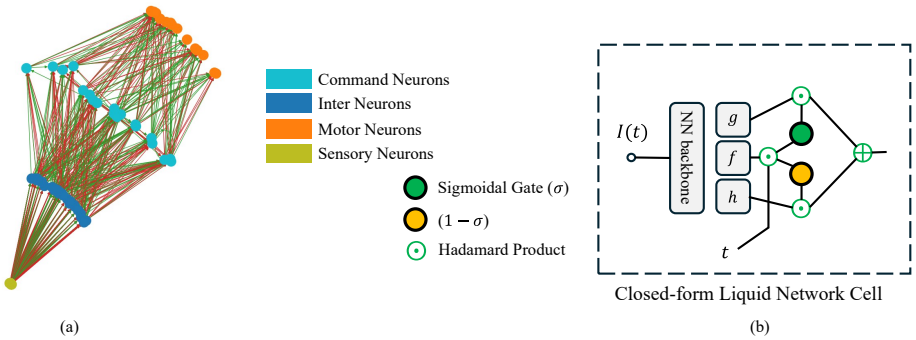


**Fig. 2.** (a) represents closed-form liquid network (CfC) used in the proposed model. The inter, command and motor neurons are made up of using the CfC cell and is shown in (b). $g$ and $h$ are two non-linear layers that control the state of the system and $f$ determines how quickly $x(t)$ transitions between them. $I_t$ is an external input. $f, g$, and $h$ have a shared backbone that is parameterized by $\theta_f, \theta_h$ and $\theta_h$ as defined in equation 1.

stable memory, effectively correcting anomalies before the decoding step. In our proposed method, the hopfield layer learns a set of prototype feature patterns during training from a shared space. The output from the image encoder and the output from LNN are projected onto a shared space and are then concatenated before passing through the Hopfield layer. Previous work from [15] shows that MHN excels when projecting input representations into a shared space for similarity-based comparison. We use the Hopfield Layer implementation to learn patterns from the concatenated feature set.

Let $p_1, p_2, \ldots, p_M$ be the learned patterns (memory vectors) stored in the Hopfield layer, and let $q = h_T$ be the query vector. The Hopfield retrieval is an associative lookup that finds the memory pattern closest to $q$ in the feature space. This can be expressed as a weighted average of all stored patterns, where weights are given by a softmax over their similarity to the query:

$$r = \sum_{j=1}^{M} \left( \frac{\sum_{k=1}^{M} \exp(\kappa \langle q, p_k \rangle)}{\exp(\kappa \langle q, p_j \rangle)} \right) p_j, \tag{2}$$

where $\langle q, p_j \rangle$ is the similarity between the query and pattern $j$, and $\kappa$ is a scaling factor that controls the sharpness of the association. This update rule is essentially equivalent to the attention mechanism used in Transformers, and indeed the MHN can be seen as performing a single-step attention-based memory retrieval. The result $r$ is the recalled pattern most consistent with $q$. This enriched representation is then forwarded to the decoder. By injecting the hopfield associative memory, the network is encouraged to produce features that match learned prototypical patterns of nuclei, which improves robustness especially un-

der out-of-distribution conditions – if the LNN produces an anomalous feature sequence, the MHN layer will pull it towards the closest stable pattern.

## 3 Experiments and Results

### 3.1 Dataset

We train our model on the PanNuke dataset [7], which offers a large-scale, diverse collection of nuclei instances across 19 different tissue types. PanNuke contains 7,904 H&E images with 205,343 annotated nuclei. This diversity and scale, with nuclei from numerous organs and pathologies, provide a strong foundation for learning robust multi-class segmentation. For evaluation, we employ three out-of-distribution test datasets (not seen during training) - CryoNuSeg [21], CoNIC [24] and CoNSeP [9]. CryoNuSeg introduces a significant domain shift as nuclei in frozen tissue sections often have blurred morphology and staining artifacts due to the freezing process. Key challenges in CoNIC include extremely high cellularity (dense clusters of nuclei) and heterogeneity across different clinical data sources, which tests the robustness of segmentation models to variations in stain and tissue preparation. On the other hand, CoNSeP images represent typical formalin-fixed paraffin-embedded (FFPE) colon tumor sections, with diverse appearance of nuclei and abundant cell overlapping. Together, these test sets span a range of tissue types and different preparation protocols, providing a rigorous evaluation of out-of-distribution segmentation performance of our approach.

### 3.2 Implementation

Our approach is implemented in PyTorch and trained on a single NVIDIA RTX A6000 GPU. For consistency, all dataset images are resized to 256×256 pixels before feeding into the network. We train the model for 50 epochs using the Adam optimizer with learning rate of $1 \times 10^{-4}$ with a batch size of 16. We adopt loss function similar to [10] for our instance segmentation task. This is a composite loss that combines multiple terms to handle per-pixel segmentation accuracy and instance separation simultaneously. We use a combination of Lovasz-Softmax loss [4] with seed and smooth loss. The Lovász-Softmax implementation sorts pixel errors and computes a piecewise linear extension of the IoU loss that helps the network to maximize overlap between predicted masks and ground truth. In order to encourage correct instance detection, we include seed loss, where we calculate the deviation of the centroids from ground truth seed masks. To enforce spatial consistency in the segmentation output, we add a smoothness regularization. This loss penalizes abrupt changes in the predicted mask probabilities between neighboring pixels. During training of LoRA-SAM, the SAM backbone was kept frozen while only the LoRA parameters were optimized. Our LNN and MHN components were trained along with the LoRA parameters while training the models.

**Table 1.** Performance comparison of various models across OOD CryoNuSeg, CoNIC, and CoNSep datasets. Frozen models were used for SAM and MedSAM as denoted by *. Ours indicates LoRA-SAM w/ LNN and MHN.

| **Datasets** | **CryoNuSeg** | | | | **CoNIC** | | | | **CoNSep** | | | |
|---|---|---|---|---|---|---|---|---|---|---|---|---|
| **Models** | **Dice** | **AJI** | **PQ** | **HD** | **Dice** | **AJI** | **PQ** | **HD** | **Dice** | **AJI** | **PQ** | **HD** |
| U-Net | 18.31 | 7.44 | 5.16 | 360.37 | 19.16 | 8.17 | 6.91 | 355.17 | 17.29 | 7.96 | 5.68 | 381.55 |
| nnU-Net | 24.79 | 18.82 | 13.68 | 244.98 | 21.46 | 18.52 | 10.30 | 322.67 | 30.32 | 21.25 | 14.61 | 218.17 |
| U-Net3+ | 41.70 | 34.95 | 21.52 | 151.60 | 40.64 | 37.88 | 22.70 | 158.19 | 36.68 | 28.83 | 14.77 | 193.34 |
| SAM* | 66.93 | 41.64 | 30.11 | 72.59 | 67.53 | 43.29 | 31.65 | 80.58 | 73.49 | 56.12 | 45.30 | 62.11 |
| MedSAM* | 75.79 | 53.29 | 42.44 | 51.18 | 71.37 | 51.44 | 40.08 | 59.77 | 76.23 | 55.87 | 44.56 | 77.09 |
| HoVer-NeXt | 76.90 | 55.36 | 46.73 | 50.24 | 72.64 | 52.57 | 41.14 | 61.23 | 77.17 | 57.21 | 47.23 | 76.37 |
| MedOoD | 78.48 | 56.14 | 48.12 | 47.06 | 73.72 | 54.06 | 43.25 | 54.40 | 79.12 | 58.95 | 49.44 | 65.58 |
| LoRA-SAM | 81.51 | 63.19 | 55.31 | 34.08 | 78.15 | 60.52 | 51.34 | 40.01 | 84.29 | 73.14 | 61.61 | 28.53 |
| **Ours** | **93.22** | **81.25** | **69.13** | **12.26** | **89.09** | **76.88** | **66.32** | **14.55** | **95.40** | **84.71** | **74.67** | **8.12** |

We evaluate segmentation performance using four metrics: Dice Score, Aggregated Jaccard Index (AJI), Panoptic Quality (PQ), and Hausdorff Distance (HD). Dice focuses on overall pixel overlap, AJI on per-instance segmentation quality (with penalties for instance assignment errors), PQ on combined detection-segmentation efficacy, and HD on boundary precision. By analyzing all four, we obtain a comprehensive assessment of our model's segmentation quality and robustness. In particular, Dice and AJI quantify general segmentation accuracy, PQ stresses the importance of correct instance count and segmentation, and HD ensures that even fine boundary details are evaluated.

**Table 2.** Effectiveness of proposed method across models on OOD CryoNuSeg dataset. Ours indicates Baseline w/ LNN and MHN.

| | **Dice** | | **AJI** | | **PQ** | | **HD** | |
|---|---|---|---|---|---|---|---|---|
| **Models** | **Baseline** | **Ours** | **Baseline** | **Ours** | **Baseline** | **Ours** | **Baseline** | **Ours** |
| U-Net | 18.31 | 51.43 | 7.44 | 32.04 | 5.16 | 26.72 | 360.37 | 77.64 |
| nnU-Net | 24.79 | 79.36 | 18.82 | 48.82 | 13.68 | 37.38 | 244.97 | 46.67 |
| U-Net3+ | 41.70 | 86.79 | 34.95 | 60.03 | 21.52 | 51.66 | 151.67 | 22.42 |
| LoRA-SAM | 81.51 | 93.22 | 63.19 | 81.25 | 55.31 | 69.13 | 34.08 | 12.26 |

shows the qualitative results of our proposed model. It can be observed that using LNN and MHN provides better performance on OOD datasets.

### 3.3 Results

We compare our proposed method against several baseline segmentation methods to demonstrate its effectiveness. The baselines include both conventional CNN-based architectures and recent transformer-based segmentation models. The U-Net based models represent established, task-specific segmentation pipelines,

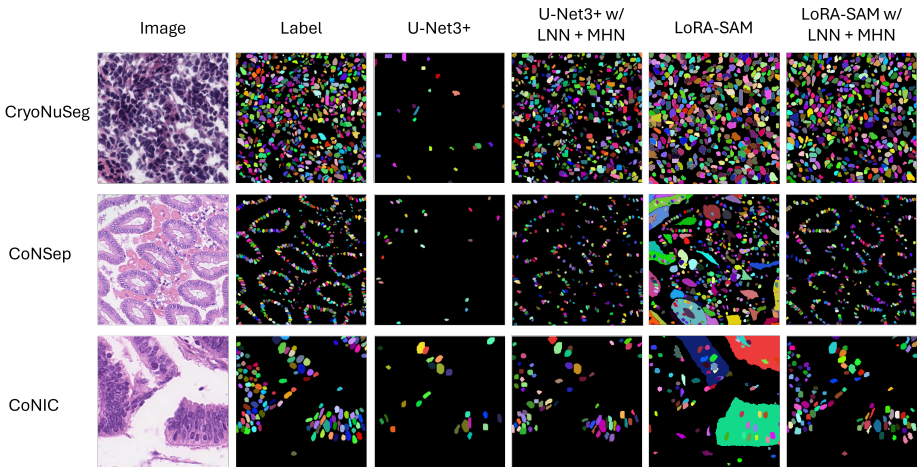


**Fig. 3.** Qualitative comparison of OOD segmentation performance of our proposed methodology with their baselines.

while SAM and its adaptations represent recent foundation model approaches leveraging transformers and prompt-based segmentation. Table 1 summarizes the performance of all methods (baselines and ours) on the three test datasets: CryoNuSeg, CoNIC, and CoNSeP. Overall, our LNN+MHN implmentation on LoRA-SAM (rank=512) demonstrates superior performance across all metrics and datasets. Not only the conventional models like U-Net struggle against the OOD datasets, foundational models too require fine-tuning to achieve comparable performance. We also compare our method with domain generalization baselines like HoVer-NeXt [3] and Med-OoD [8], where our method performed better in comparison. Furthermore, Table 2 shows that our proposed methodology achieves average performance increase of 36% in terms of dice scores, 24% in terms of AJI and 22% in terms of PQ over baseline models. In contrast to these significant gains on OOD data, the performance improvement over the baseline was marginal on the in-distribution dataset.

**Table 3.** Effect of LNN and MHN on LoRA-SAM model performance with CryoNuSeg dataset.

| Row | LNN | MHN | Dice | AJI | PQ | HD |
|---|---|---|---|---|---|---|
| 1 | - | - | 81.51 | 63.19 | 55.31 | 34.08 |
| 2 | ✓ | - | 82.36 | 65.74 | 55.58 | 33.62 |
| 3 | - | ✓ | 84.79 | 69.41 | 58.93 | 26.17 |
| 4 | ✓ | ✓ | 93.22 | 81.25 | 69.13 | 12.26 |

Table 3 shows the ablation study results. It shows the effects of LNN and MHN on LoRA-SAM model when inferenced with OOD CryoNuSeg dataset.

The results show that there is an increase in model performance when using LNN alone of about 1.03%. But when used with MHN the average performance in creases by 5.26%. However, when both LNN and MHN are used together, the performance of the model increases by 16.35% on average. This indicates that LNN and MHN complement each other. The LNN enhances feature representation and together with image encodings that provide segmentation detail to the MHN layer, the models show huge improvement in performance measures. Fig 3

## 4 Conclusion

In this study, we presented a novel framework for out-of-distribution nuclei segmentation that combines the adaptive dynamics of LNNs with the associative memory of a modern hopfield network. By processing hierarchical image features through time-aware liquid dynamics and stabilizing them with learned feature patterns, our approach achieves superior segmentation accuracy across diverse histopathology datasets. Extensive experiments demonstrate that our method consistently outperforms strong baselines, highlighting its robustness to domain shifts. Our proposed model increases the model performance by 16.35% highlighting the effectiveness of our approach. The major limitations include high training time due to LNN iterations which we plan to mitigate in future studies. Our work offers a promising direction for building more adaptable and generalizable segmentation models in computational pathology.

**Acknowledgments.** This research was supported by BL Science grants (202301630001).

**Disclosure of Interests.** The authors have no competing interests to declare that are relevant to the content of this article.

## References

1. Akpinar, M.H., Atila, O., Sengur, A., Salvi, M., Acharya, U.: A novel uncertainty-aware liquid neural network for noise-resilient time series forecasting and classification. Chaos, Solitons & Fractals **193**, 116130 (2025), https://www.sciencedirect.com/science/article/pii/S0960077925001432
2. Archit, A., Freckmann, L., Nair, S., Khalid, N., Hilt, P., Rajashekar, V., Freitag, M., Teuber, C., Buckley, G., von Haaren, S., Gupta, S., Dengel, A., Ahmed, S., Pape, C.: Segment anything for microscopy. Nature Methods (Feb 2025)
3. Baumann, E., Dislich, B., Rumberger, J.L., Nagtegaal, I.D., Martinez, M.R., Zlobec, I.: Hover-next: A fast nuclei segmentation and classification pipeline for next generation histopathology. In: Medical Imaging with Deep Learning (2024)
4. Berman, M., Triki, A.R., Blaschko, M.B.: The lovász-softmax loss: A tractable surrogate for the optimization of the intersection-over-union measure in neural networks (2018), https://arxiv.org/abs/1705.08790
5. Chahine, M., Hasani, R., Kao, P., Ray, A., Shubert, R., Lechner, M., Amini, A., Rus, D.: Robust flight navigation out of distribution with liquid neural networks. Sci. Robot. **8**(77), eadc8892 (apr 2023)

6. Chen, Z., Xu, Q., Liu, X., Yuan, Y.: Un-sam: Universal prompt-free segmentation for generalized nuclei images (2024), https://arxiv.org/abs/2402.16663
7. Gamper, J., Koohbanani, N.A., Benes, K., Khuram, A., Rajpoot, N.: Pannuke: an open pan-cancer histology dataset for nuclei instance segmentation and classification. In: European Congress on Digital Pathology. pp. 11–19. Springer (2019)
8. Gao, Y., Xu, D.: Out-of-distribution data supervision towards biomedical semantic segmentation. In: Zhao, H., Chen, L. (eds.) Fifth International Conference on Signal Processing and Computer Science (SPCS 2024). vol. 13442, p. 1344208. International Society for Optics and Photonics, SPIE (2025). https://doi.org/10.1117/12.3052988, https://doi.org/10.1117/12.3052988
9. Graham, S., Vu, Q.D., Raza, S.E.A., Azam, A., Tsang, Y.W., Kwak, J.T., Rajpoot, N.: Hover-net: Simultaneous segmentation and classification of nuclei in multi-tissue histology images. Medical Image Analysis **58**, 101563 (2019), https://www.sciencedirect.com/science/article/pii/S1361841519301045
10. Gudhe, N.R., Kosma, V.M., Behravan, H., Mannermaa, A.: Nuclei instance segmentation from histopathology images using bayesian dropout based deep learning. BMC Medical Imaging **23**(1), 162 (Oct 2023)
11. Hasani, R., Lechner, M., Amini, A., Liebenwein, L., Ray, A., Tschaikowski, M., Teschl, G., Rus, D.: Closed-form continuous-time neural networks. Nature Machine Intelligence **4**(11), 992–1003 (Nov 2022)
12. Hasani, R., Lechner, M., Amini, A., Rus, D., Grosu, R.: Liquid time-constant networks (2020), https://arxiv.org/abs/2006.04439
13. Hoque, M.Z., Keskinarkaus, A., Nyberg, P., Seppänen, T.: Stain normalization methods for histopathology image analysis: A comprehensive review and experimental comparison. Information Fusion **102**, 101997 (2024), https://www.sciencedirect.com/science/article/pii/S1566253523003135
14. Hörst, F., Rempe, M., Heine, L., Seibold, C., Keyl, J., Baldini, G., Ugurel, S., Siveke, J., Grünwald, B., Egger, J., Kleesiek, J.: Cellvit: Vision transformers for precise cell segmentation and classification. Medical Image Analysis **94**, 103143 (2024), https://www.sciencedirect.com/science/article/pii/S1361841524000689
15. Kashyap, S., D'Souza, N.S., Shi, L., Wong, K.C.L., Wang, H., Syeda-Mahmood, T.: Modern hopfield networks meet encoded neural representations – addressing practical considerations (2024), https://arxiv.org/abs/2409.16408
16. Kirillov, A., Mintun, E., Ravi, N., Mao, H., Rolland, C., Gustafson, L., Xiao, T., Whitehead, S., Berg, A.C., Lo, W.Y., Dollár, P., Girshick, R.: Segment anything (2023)
17. Kumar, N., Verma, R., Sharma, S., Bhargava, S., Vahadane, A., Sethi, A.: A dataset and a technique for generalized nuclear segmentation for computational pathology. IEEE Trans. Med. Imaging **36**(7), 1550–1560 (jul 2017)
18. Li, C., Liu, D., Li, H., Zhang, Z., Lu, G., Chang, X., Cai, Weidong", e.L., Dou, Q., Fletcher, P.T., Speidel, S., Li, S.: Domain adaptive nuclei instance segmentation and classification via category-aware feature alignment and pseudo-labelling. In: Medical Image Computing and Computer Assisted Intervention – MICCAI 2022. pp. 715–724. Springer Nature Switzerland, Cham (2022)
19. Lou, Z., Xu, Q., Jiang, Z., He, X., Chen, Z., Wang, Y., Li, C., He, M.M., Duan, W.: Nusegdg: Integration of heterogeneous space and gaussian kernel for domain-generalized nuclei segmentation (2024), https://arxiv.org/abs/2408.11787
20. Mahbod, A., Dorffner, G., Ellinger, I., Woitek, R., Hatamikia, S.: Improving generalization capability of deep learning-based nuclei instance segmentation by non-deterministic train time and deterministic test time stain normalization. Computational and Structural Biotechnology Journal **23**, 669–678 (Dec 2024)

21. Mahbod, A., Schaefer, G., Bancher, B., Löw, C., Dorffner, G., Ecker, R., Ellinger, I.: Cryonuseg: A dataset for nuclei instance segmentation of cryosectioned h&e-stained histological images. Computers in Biology and Medicine **132**, 104349 (2021), https://www.sciencedirect.com/science/article/pii/S0010482521001438
22. Ramsauer, H., Schäfl, B., Lehner, J., Seidl, P., Widrich, M., Adler, T., Gruber, L., Holzleitner, M., Pavlović, M., Sandve, G.K., Greiff, V., Kreil, D., Kopp, M., Klambauer, G., Brandstetter, J., Hochreiter, S.: Hopfield networks is all you need (2021), https://arxiv.org/abs/2008.02217
23. Ronneberger, O., Fischer, P., Brox, T.: U-net: Convolutional networks for biomedical image segmentation (2015)
24. Simon Graham, e.a.: Conic challenge: Pushing the frontiers of nuclear detection, segmentation, classification and counting (2023), https://arxiv.org/abs/2303.06274
25. Swain, B.R., Cheoi, K.J., Ko, J.: Sam guided task-specific enhanced nuclei segmentation in digital pathology. In: Medical Image Computing and Computer Assisted Intervention – MICCAI 2024. pp. 542–551. Springer Nature Switzerland, Cham (2024)
26. Voon, W., Hum, Y.C., Tee, Y.K., Yap, W.S., Nisar, H., Mokayed, H., Gupta, N., Lai, K.W.: Evaluating the effectiveness of stain normalization techniques in automated grading of invasive ductal carcinoma histopathological images. Scientific Reports **13**(1), 20518 (Nov 2023)
27. Wang, J., Kwak, J.T.: Nucleimix: Realistic data augmentation for nuclei instance segmentation (2024), https://arxiv.org/abs/2410.16671
28. Wang, S., Rong, R., Gu, Z., Fujimoto, J., Zhan, X., Xie, Y., Xiao, G.: Unsupervised domain adaptation for nuclei segmentation: Adapting from hematoxylin & eosin stained slides to immunohistochemistry stained slides using a curriculum approach. Computer Methods and Programs in Biomedicine **241**, 107768 (2023), https://www.sciencedirect.com/science/article/pii/S0169260723004340
29. Zingman, I., Frayle, S., Tankoyeu, I., Sukhanov, S., Heinemann, F.: A comparative evaluation of image-to-image translation methods for stain transfer in histopathology. In: Oguz, I., Noble, J., Li, X., Styner, M., Baumgartner, C., Rusu, M., Heinmann, T., Kontos, D., Landman, B., Dawant, B. (eds.) Medical Imaging with Deep Learning. Proceedings of Machine Learning Research, vol. 227, pp. 1509–1525. PMLR (10–12 Jul 2024), https://proceedings.mlr.press/v227/zingman24a.html